nature portfolio

https://doi.org/10.1038/s41586-022-05024-1

Supplementary information

Exciton-coupled coherent magnons in a 2D semiconductor

In the format provided by the authors and unedited

SUPPORTING INFORMATION

Exciton-Coupled Coherent Magnons in a 2D Semiconductor

Youn Jue Bae[1], Jue Wang[1], Allen Scheie[2], Junwen Xu[3], Daniel G. Chica[1], Geoffrey M. Diederich[4,5], John Cenker[4], Michael E. Ziebel[1], Yusong Bai[1], Haowen Ren[3], Cory R. Dean[6], Milan Delor[1], Xiaodong Xu[4], Xavier Roy[1], Andrew D. Kent[3], Xiaoyang Zhu[1,1]

[1] Department of Chemistry, Columbia University, New York, NY 10027, USA
[2] Neutron Scattering Division, Oak Ridge National Laboratory, Oak Ridge, TN 37831, USA
[3] Department of Physics, New York University, New York, NY, USA 10003, USA
[4] Department of Physics, University of Washington, Seattle, WA 98195, USA
[5] Intelligence Community Postdoctoral Research Fellowship Program, University of Washington, Seattle, WA 98195, USA
[6] Department of Physics and Astronomy, Columbia University, New York, NY 10027, USA

[1] To whom correspondence should be addressed. E-mail: xyzhu@columbia.edu

Supplementary Information Guide

SI References

1. Wang, J. *et al.* Optical generation of high carrier densities in 2D semiconductor heterobilayers. *Sci. Adv.* **5**, eaax0145 (2019).
2. Wang, J. *et al.* Diffusivity Reveals Three Distinct Phases of Interlayer Excitons in MoSe2/WSe2 Heterobilayers. *Phys. Rev. Lett.* **126**, 106804 (2021).
3. Holstein, T. & Primakoff, H. Field Dependence of the Intrinsic Domain Magnetization of a Ferromagnet. *Phys. Rev.* **58**, 1098–1113 (1940).
4. Toth, S. & Lake, B. Linear spin wave theory for single-Q incommensurate magnetic structures. *J. Phys. Condens. Matter* **27**, 166002 (2015).
5. Scheie, A. *et al*. Spin waves and magnetic exchange Hamiltonian in CrSBr. *arXiv preprint arXiv:2204.12461* (2022).
6. MacNeill, D. *et al.* Gigahertz Frequency Antiferromagnetic Resonance and Strong Magnon-Magnon Coupling in the Layered Crystal CrCl3. *Phys. Rev. Lett.* **123**, 47204 (2019).

1. Temperature dependent ΔR/R spectra

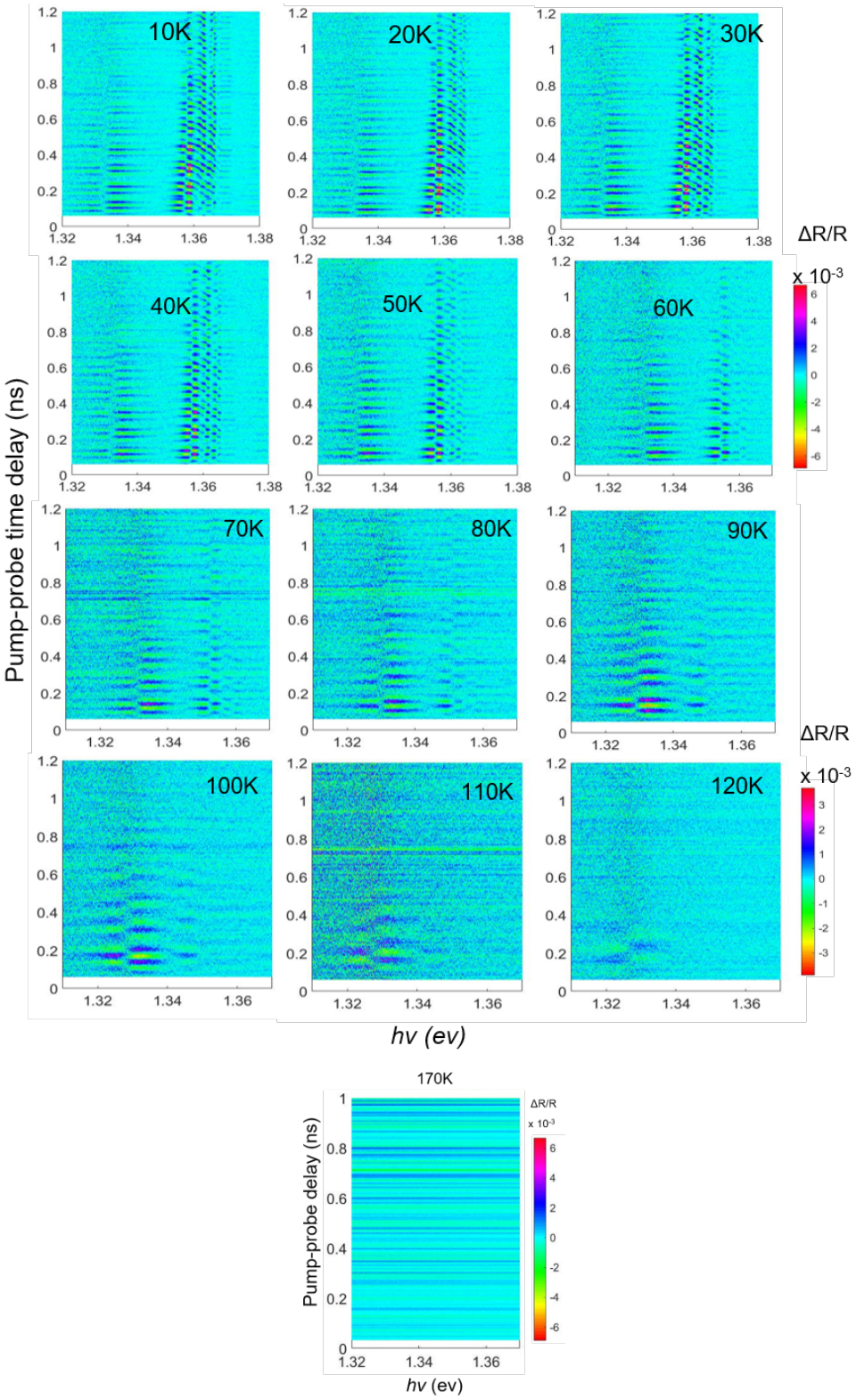

Fig. S1. ΔR/R spectra at different temperatures below and above the Neel temperature (T_N = 135K).

2. ΔR/R spectra with zero magnetic field

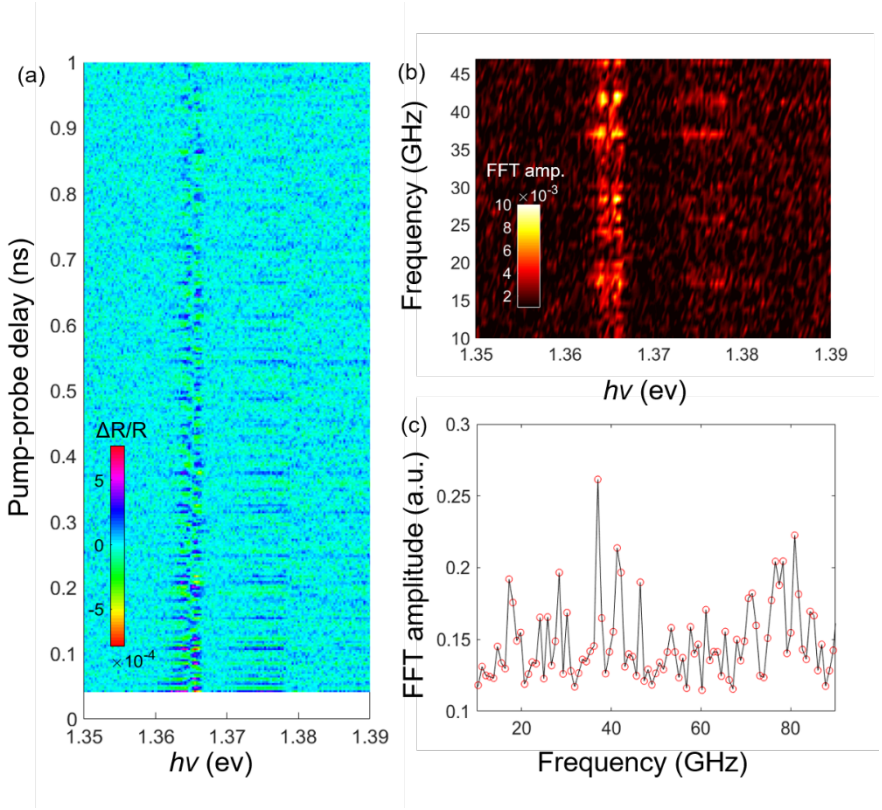

Fig. S2. (a) ΔR/R spectra without the incoherent electronic signal (b) FFT frequency vs. probe photon energy (*hv*) and (c) the summation of the FFT amplitude from (b) at $B_0 = 0$ T.

3. Exciton energy modulation by coherent spin waves in bulk CrSBr samples. We estimate the energy modulation of excitons in the CrSBr bulk sample (Fig. S3) by adding scaled steady state reflectance to the ΔR/R spectra. Here, we subtract the incoherent electronic signal from the raw ΔR/R spectra. The resulting subtracted spectra at different probe wavelengths are shown in Fig. S8. The time-dependent spectral change of the minimum and the maximum of the subtracted ΔR/R spectra can be approximated as the magnitude of the energy modulation (Fig. S4). Taking the FFT of the energy modulation, we obtain the two magnon frequencies, 24 and 34 GHz. We quantify the magnitude of the modulated exciton energy by adding the steady state reflectance spectra to the subtracted ΔR/R spectra (Fig. S5). The phase flip in the signal can be understood as the exciton energy moving to the left or right with respect to the exciton energy at time 0. For bulk CrSBr, the measured change in exciton energy is 0.9 meV in the 1.358 eV region and 3.2 meV in the 1.340 eV region.

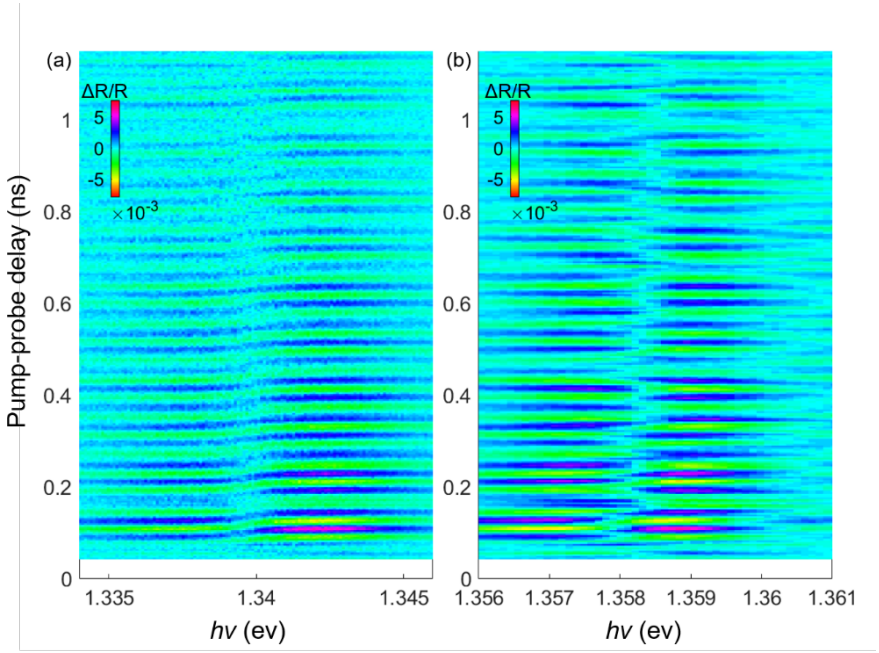

Fig. S3. Transient reflectance spectra around the exciton energy of (a) 1.340 eV and (b) 1.358 eV.

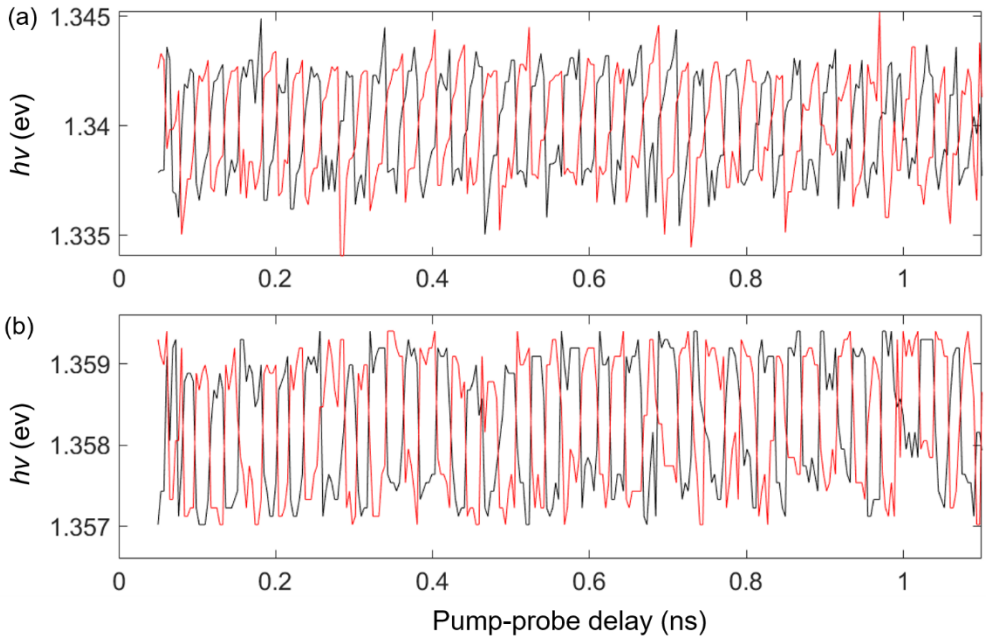

Fig. S4. Time dependent traces of maximum (black) and minimum (red) peak of the ΔR/R at (a) 1.358 eV and (b) 1.340 eV.

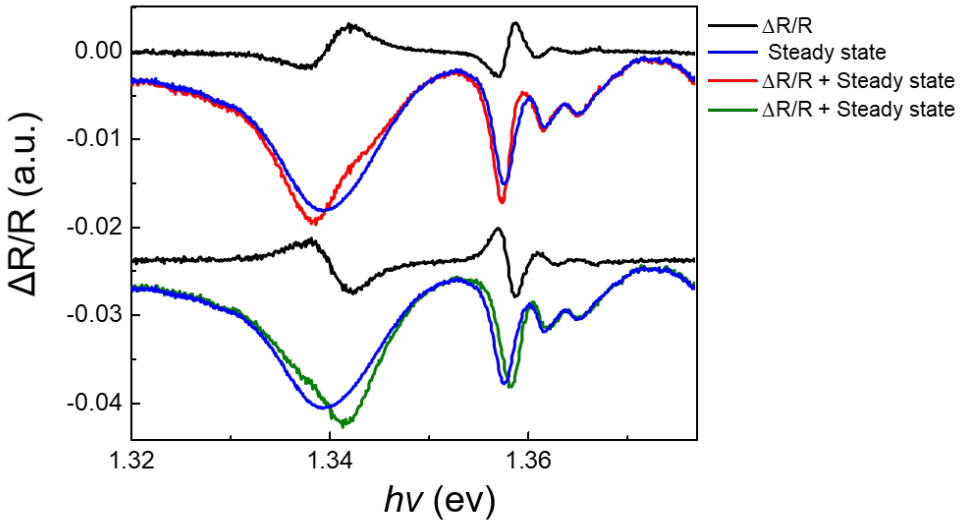

Fig. S5. Addition of the scaled steady state reflectance spectra to the subtracted ΔR/R spectra.

4. AFMR spectral analysis and temperature dependence.

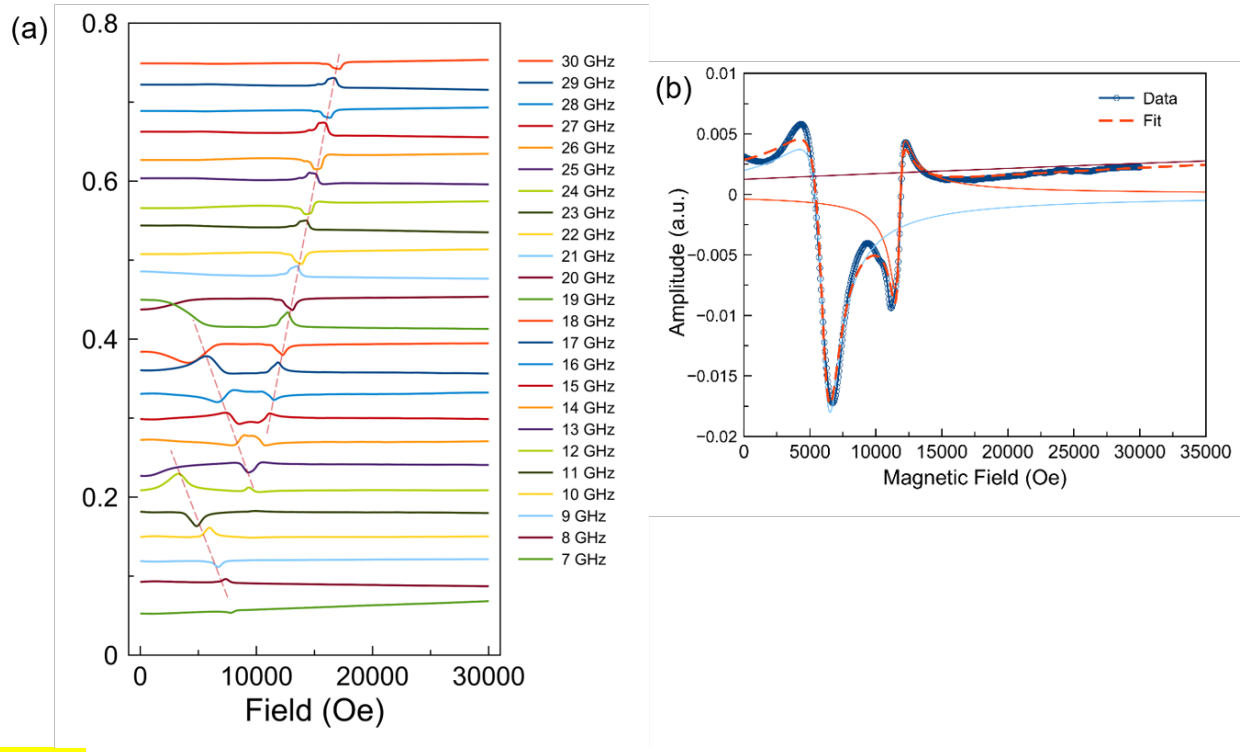

Fig. S6. (a) The real part of the spectra of S12, transmission port at different resonance frequencies at 100K. (b) Peak fitting using a linear combination of symmetric and antisymmetric Lorentzian functions.

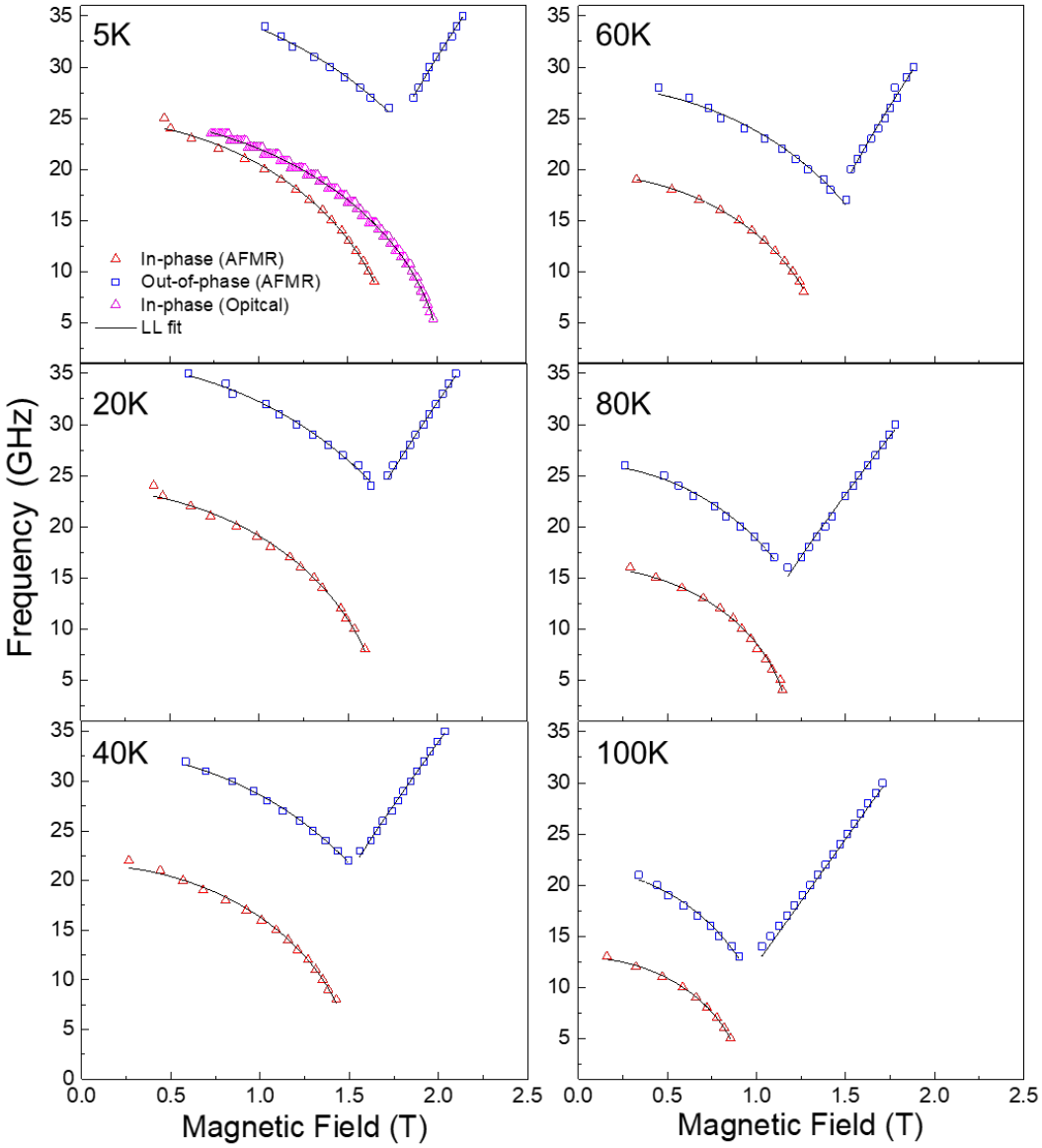

Fig. S7. AFMR frequency vs. magnetic field plots at different temperatures. Note, the saturation field is decreasing with the temperature.

5. Coherent spin wave propagation analysis. The probe-wavelength dependent short time Fourier transform (STFT) is performed at a fixed frequency of 2 GHz, 24 GHz and 34 GHz along both a and b-axis. Using the MATLAB built in STFT function, time window of 600 ps and a hamming window of 590 ps are used for 2 GHz mode. For 24 GHz and 34 GHz, time window of 150 ps with a hamming window of 140 ps is used. The rise and decay of the STFT indicates that magnons are propagating coherently. At a longer probe distance, the width of the amplitude gets broader and the amplitude decays as the propagating magnons lose temporal and spatial coherence. The group velocities of magnon and phonon are obtained from the linear fitting of the pump-probe distance (d) v.s. pump-probe time delay.

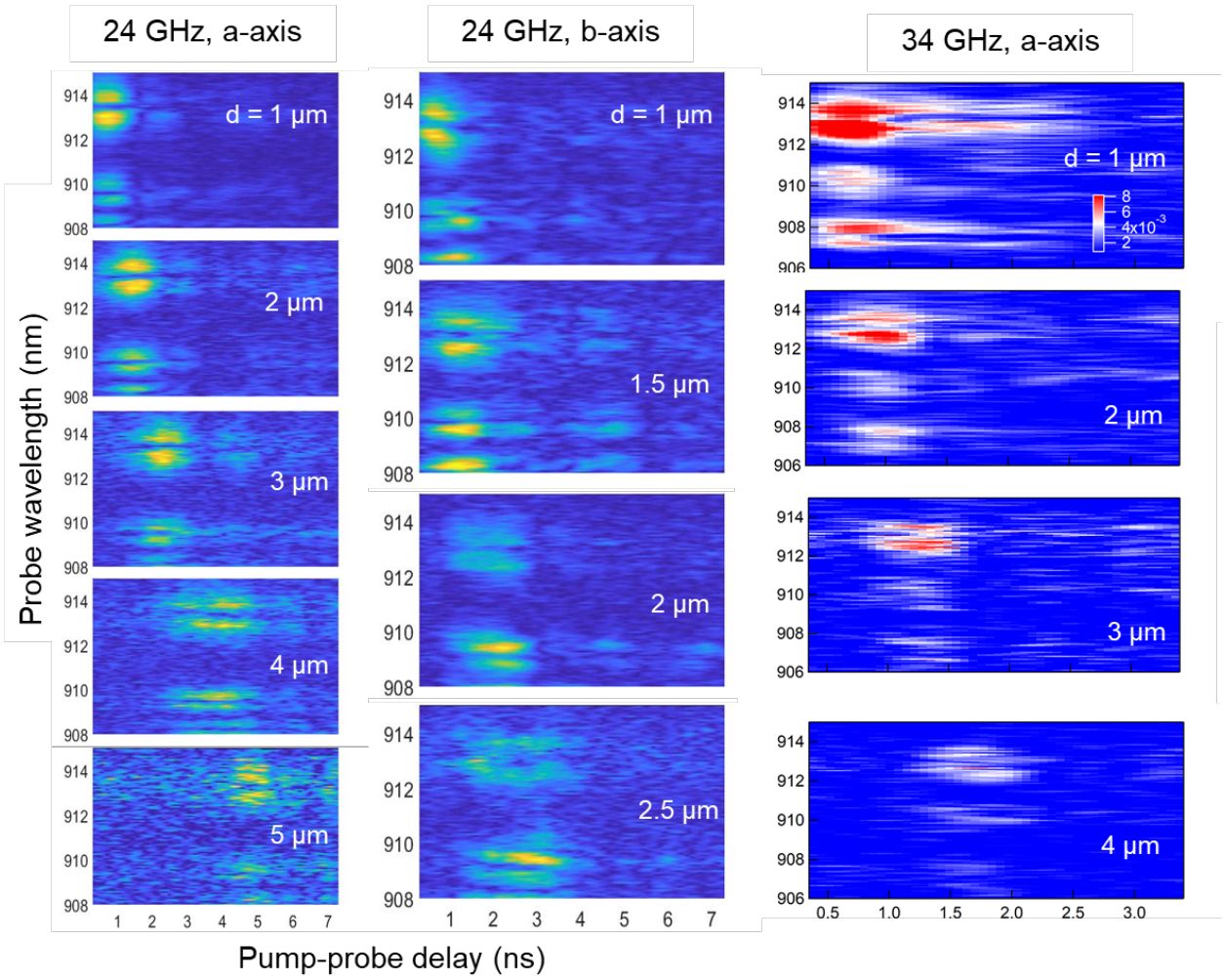

Fig. S8. STFT spectra of 24 GHz and 34 GHz magnon modes along the *a*- and *b*-axis of the bulk CrSBr.

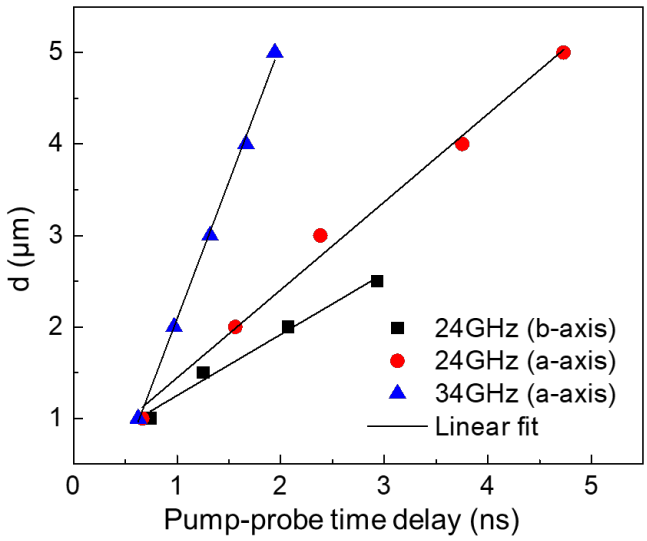

Fig. S9. Pump-probe distance (d) vs. time delay for magnon modes with group velocities, $V_g = 1.0 \pm 0.1$ and 3.0 ± 0.3 km/s, for the 24, 34 GHz along the *a*-axis, respectively and $V_g = 0.7 \pm 0.1$ for the 24 GHz mode along the *b* -axis

6. Magnon peak splitting in the frequency domain. As discussed in the main text, magnon peaks split into two peaks and the width of the two peaks depends on the probe wavelength. For instance, at 908.5 nm 910.4 nm and 912.9 nm, the splitting width is 0.93 GHz, 0.93 GHz and 0.4 GHz for 24 GHz and 0.4 GHz, 1 GHz and 0.53 GHz for 34 GHz.

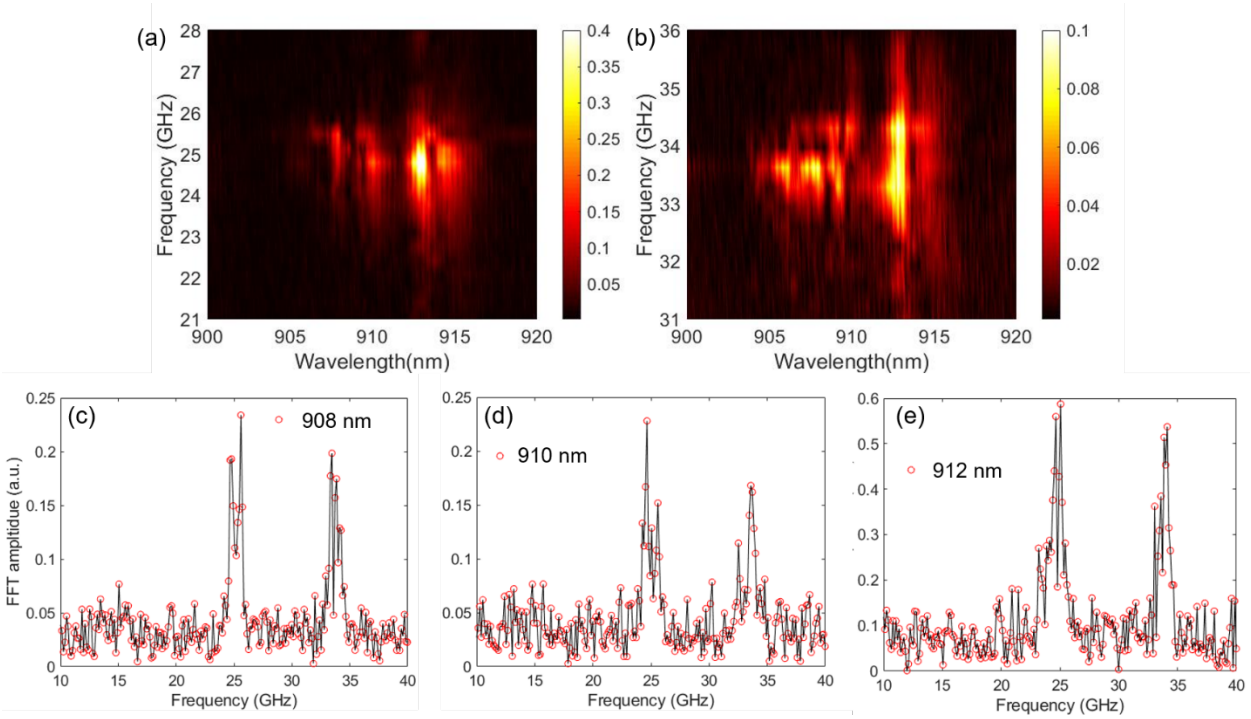

Fig. S10. FFT spectra of the two magnon. (a) 24 GHz and (b) 34 GHz modes show peak splitting at (c), (d), and (e) different probe wavelengths.

7. Magnon peak width analysis. We determine the coherence lifetime from the full-width-half-maximum (FWHM) of the Lorentzian peak fitting. The time step is 4 ps and the number of data points are 1950, thus the frequency resolution is 0.1 GHz. From Lorentzian peak fitting, we obtain three peaks, 25.7 ± 0.1, 24.5 ± 0.2, and 34.7 ± 0.2. The FWHM of the three peaks corresponds to 0.2 GHz, 0.4 GHz and 0.4 GHz which translate into 5 ns, 2.5 ns and 2.5 ns.

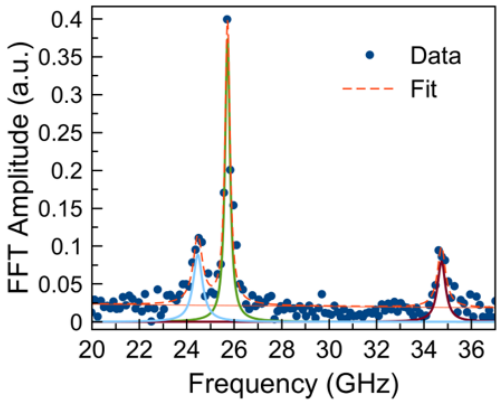

Fig. S11. Lorentzian peak fitting of the FFT spectra averaged over the entire probe photon energy.

8. Energy modulation in a few layer CrSBr flakes. The same analysis is applied to a few layers of CrSBr samples (Figures S11-S14). Unlike the bulk sample, a few layers CrSBr samples contain one major exciton peak around 910 nm. Although the amplitude of magnon oscillation is large at a single probe wavelength down to the trilayer CrSBr, the amplitude is small in the bilayer. Therefore, the magnon frequencies in the bilayer sample are integrated over the entire exciton peak. Thus, the magnitude of the energy modulation cannot be identified for bilayers but magnon frequencies can be still detected. Note the representative data set is shown below and the error bars come from an average of 2-3 different flakes.

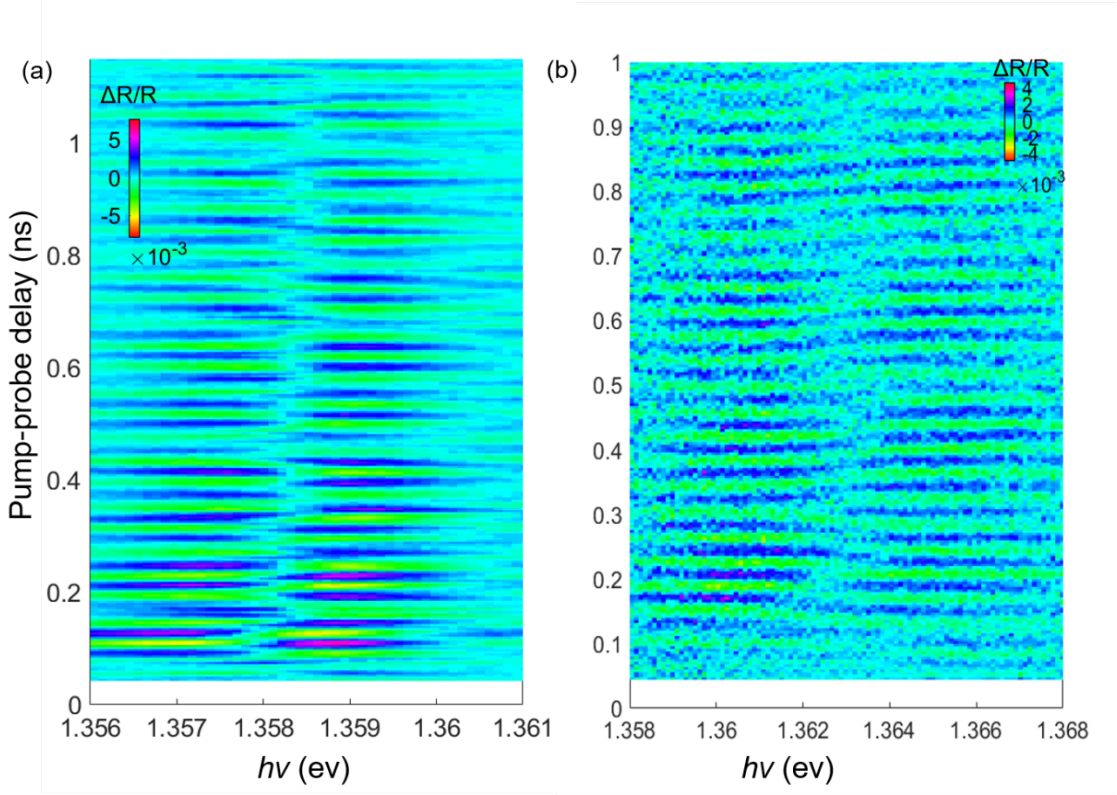

Fig. S12. Transient reflectance spectra of (a) 4L and (b) 3L after the subtraction of incoherent electronic signals. The corresponding spectrum for 5L is shown in the main text Fig. 4a.

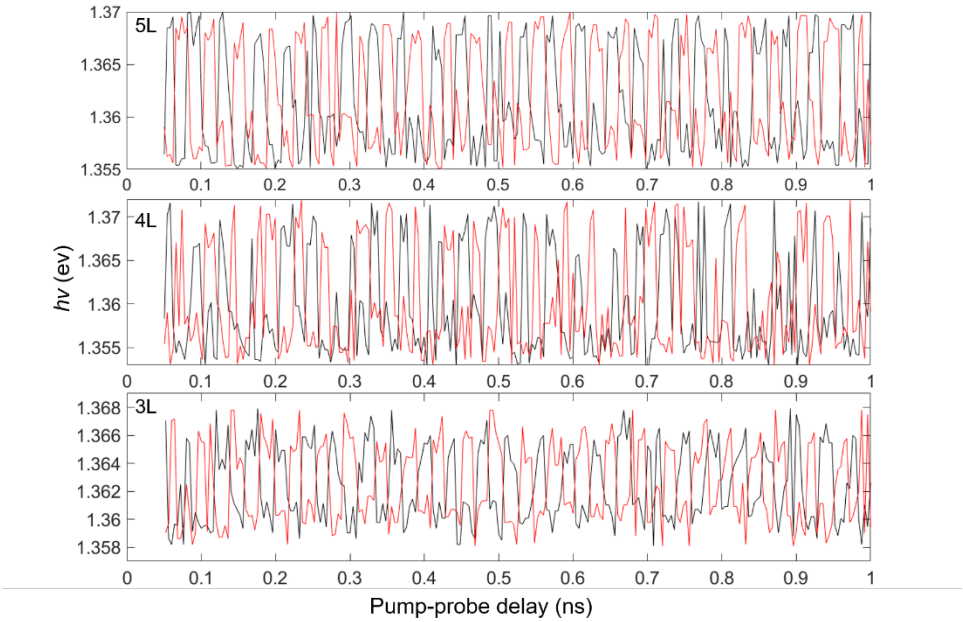

Fig. S13. Time dependent traces of maximum (black) and minimum (red) peak of the subtracted ΔR/R.

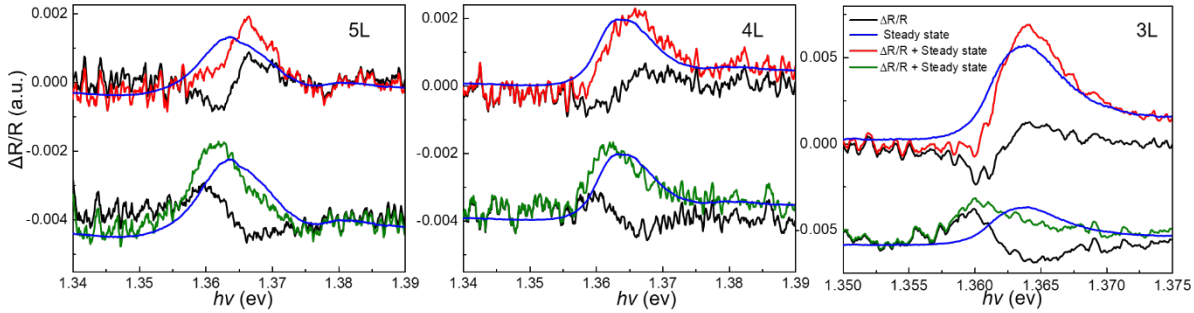

Fig. S14. Addition of the scaled steady state reflectance spectra to the subtracted ΔR/R spectra.

Table S1. Magnon frequencies and energy modulation.

Sample	Energy modulation (meV)
Bulk	3.2 ± 0.6
5L	5.1 ± 0.5
4L	3.7 ± 0.4
3L	4.0 ± 0.7

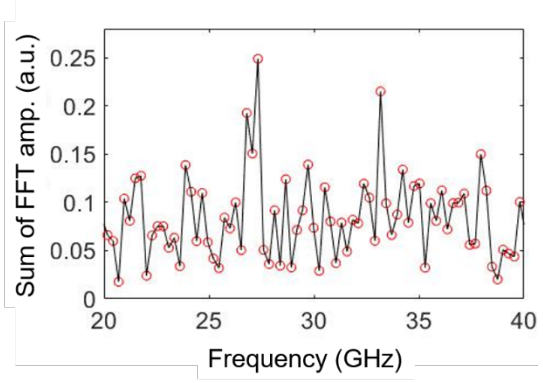

Figs. S15. FFT spectrum averaged over the entire probe photon energy of 2L.

9. Coherence time for 5L sample

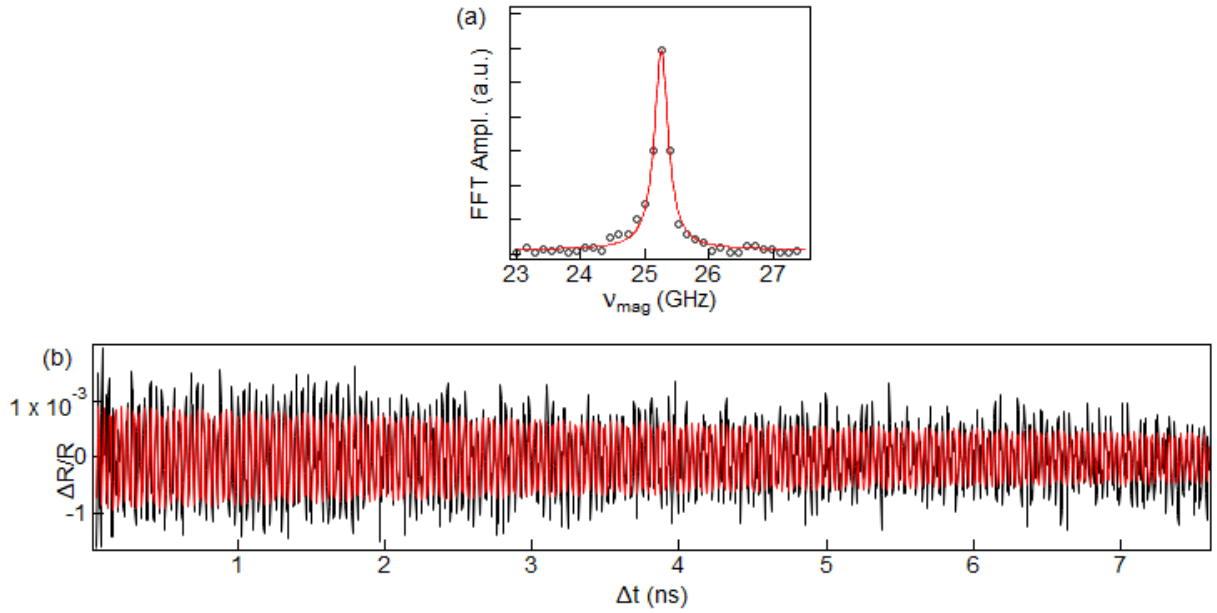

Fig. S16. FFT spectrum of the (a) 24 GHz mode of the 5L sample discussed in main text Fig. 5b and (b) time domain oscillating signal (black) with damped sine wave fitting (red). FFT peak fitting gives a full-width-at-half-maximum of 0.20±0.02 GHz, which corresponds to decoherence time of 5 ±0.5 ns and damped sine wave fitting gives decoherence time of 10 ± 1 ns. Note, this sample has the longest coherence time among 3 different 5L samples.

10. Optical and AFM images

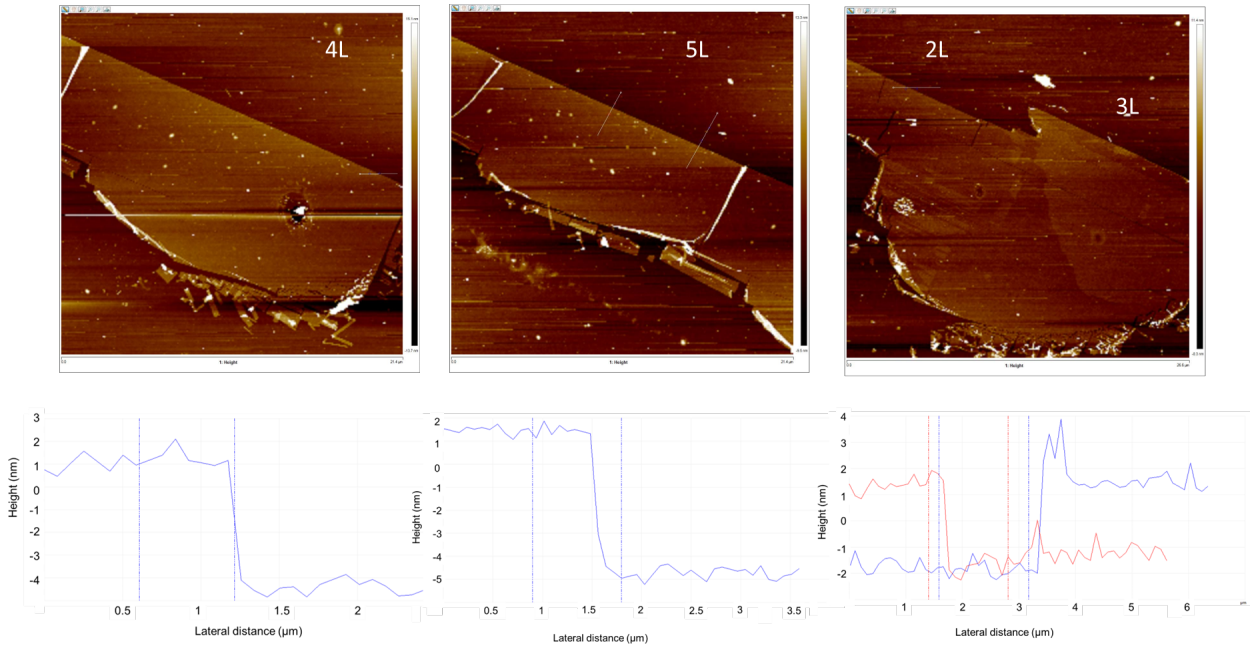

Fig. S17. (Top) AFM images of a few layers of CrSBr flakes. (Bottom) Linecuts from the height images.

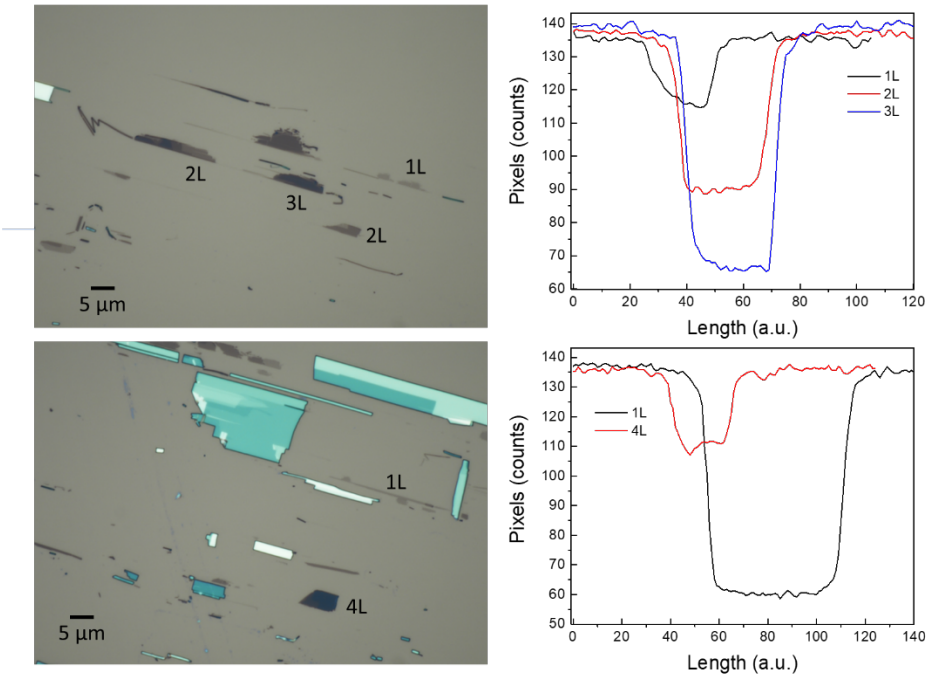

Fig. S18. (Left) Optical images of bulk and a few layers of CrSBr flakes. (Right) Optical contrast from the images shown on the left.

11. Description of optical set up.

Transient reflectance spectroscopy and microscopy at 0.2 T. A close-cycle liquid helium cryostat (Montana) is used to cool the temperature down to 4K. A permanent magnet is attached to the sample holder using epoxy glue to achieve 0.2 T at the sample position. The magnetic field at the sample position is measured at room temperature using a magnetometer (Extech SDL900). The steady state reflectance is measured using a 3200K halogen lamp (KLS EKE/AL). The broadband white light reflected from the CrSBr sample and the substrate are collected by an InGaAs photodiode array (PyLoN-IR, Princeton Instruments).

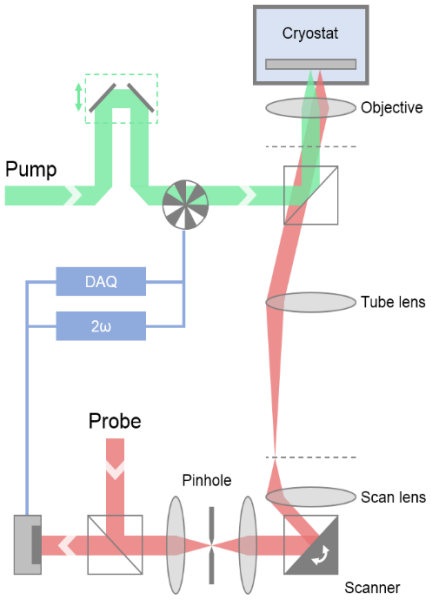

Fig. S19. Schematic illustration of pump-probe confocal optical microscope.

The detailed description of the transient reflectance set up is discussed previously.[1] Briefly, femtosecond laser pulses from the Ti:sapphire regenerative amplifier (Coherent RegA 9050, 250 kHz, 800 nm, 100 fs) is split into two beams: one for the tunable pump (Coherent OPA 9450) and the other for the broadband white light. A sapphire crystal is used to generate probe beam. The pump pulse is delayed using a motorized delay stage up to 7 ns and modulated using an optical copper to record pump-on and pump-off reflected signal using the InGaAs detector. The difference signal is normalized with the pump-off signal to yield $\Delta R/R$. The pump and the probe beam get combined using a 50:50 beam splitter in front of an objective lens. A dual-axis galvo mirror

scanning system is used to locate a probe pulse a few μm distance away from the pump pulse (Figure S3). The detailed description is written elsewhere.[2] Although the angle of incidence of the probe pulse at the back focal plane of an objective changes during the scanning process, the angle of incidence to the sample plane is kept normal for both the probe and pump pulse. Since the numerical aperture of the objective is high, the angle of incidence spans from -45° to 45°. Reflected pump and probe pulse travels the same path and the pump pulse is removed using a 800nm long pass filter.

Magneto-optical Kerr effect (MOKE). For MOKE imaging measurement shown in Fig. 3f, a pre-amplified balanced detector (PDB210A, Thorlabs), lock-in amplifier (SR830, Stanford research systems) with a chopper frequency as a reference frequency and a half-waveplate were used. A 880nm bandpass filter with the 70nm full-width-half-maximum (FWHM) was used for the broadband white light and 740 nm pump pulse from the OPA was used to excited the sample at 5K. Both the pump and probe beams pass through the same Glan-Taylor polarizer (polarized along the *b*-axis of the crystal). A 50:50 beam splitter was placed between the objective and the Glan-Taylor polarizer to direct the reflected beam into a balanced detector passing thorough a 800 nm longpass filter, half-waveplate, Wollaston prism, and a lens. Here, the probe beam travels through a dual-axis galvo scanning mirrors to precisely control the position with respect to the pump beam and to collect the pump-induced change in Kerr rotation.

Transient reflectance with variable magnetic field. For transient reflectance measurements, the 930 nm pulses from a 76 MH_z Ti:Sapph oscillator were focused into a BBO crystal to produce 465 nm SHG which was then separated from the fundamental by a dichroic beam-splitter. The 930 probe pulses were delayed via retroreflectors on a mechanical delay line, attenuated, and polarized along the *b* axis of the sample crystal. The 465 pump pulses were sent through a mechanical chopper, attenuated, and polarized before being recombined with the probe pulses and sent to a 0.6 NA microscope objective where they were focused to a spot size of ~2 micron on the sample. The reflected pulses were picked off by an OD 3 reflective neutral density filter and sent through a Wollaston prism to separate orthogonal polarization states and each beam was passed through an absorptive long pass filter and lightly focused onto one of two detectors on a balanced photoreceiver. The signal is then sent to a lock-in amplifier, demodulating at the frequency of the mechanical chopper to ensure that only the pump-induced signal change is measured.

To generate delays and measure the dynamics, the stage is continuously swept across its range at low speed while the lock-in amplifier streamed the demodulated data to the host computer. Such scans (typically N > 25) are collected and averaged to form the final data set, with the delay calculated from the stage speed, its initial position, and the measured timebase of the lock-in amplifiers internal clock. Each photodiode on the balanced detector is sent to a different lock-in channel and their sum provides the transient reflectance.

For magnetic field measurements, the cryostat used has an integrated superconducting magnet capable of applying 5 Tesla in the *z* direction across all temperatures (base temperature is ~2K). This introduces polarization rotations due to the Faraday effect in the objective glass, which we measure and correct with half waveplates in the pump, probe, and signal beam paths.

12. Spectral analysis and pump power dependence of transient reflectance data at 0.2 T.

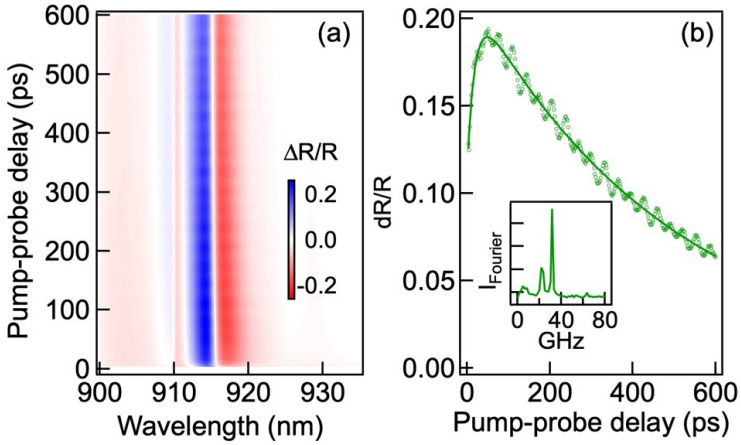

Fig. S20. (a) Transient reflectance spectra as a function of pump-probe delay and probe wavelength for a bulk CrSBr crystal at 5 K and with an external canting field, B_o = 0.2 T applied along the *c*-axis (normal to the 2D planes. The pump pulse at $h\nu_1$ = 1.7 eV (pulse width: 150 fs, rep-rate 250 kHz, power 1 μW, spot diameter: 1.4 μm) and the probe pulse at $h\nu_2$ = 1.3 – 1.4 eV (pulse width ~100 fs, power 0.2 μW, spot diameter ~1.2 μm) are used. (b) a vertical cut of the transient reflectance in (a) at 909 nm (green circles). The solid curve is a fit of the data to a gaussian convoluted with a bi-exponential decay to account for the smooth background attributed to excitonic excitation. Subtraction of the data by the smooth fit leaves the oscillatory part, whose Fourier transform yields the frequency spectrum in the inset. The subtraction the smooth background is done at every probe wavelength to yield the Δ*R/R* spectra in Fig. 1c.

Power dependence and polarization dependence. At low power the magnon FFT amplitude linearly increases with the pump power but eventually plateaus. The pump power has a minimal effect in magnon frequency. In addition to the pump power dependence, we also use linearly polarized pump along the b- and a-axis using the same pump power (0.4 μW). Since the transition dipole is along the b-axis, more excitons are formed when pump beam is polarized along the b-axis. In addition, decreased amplitude is also observed with a circularly polarized light.

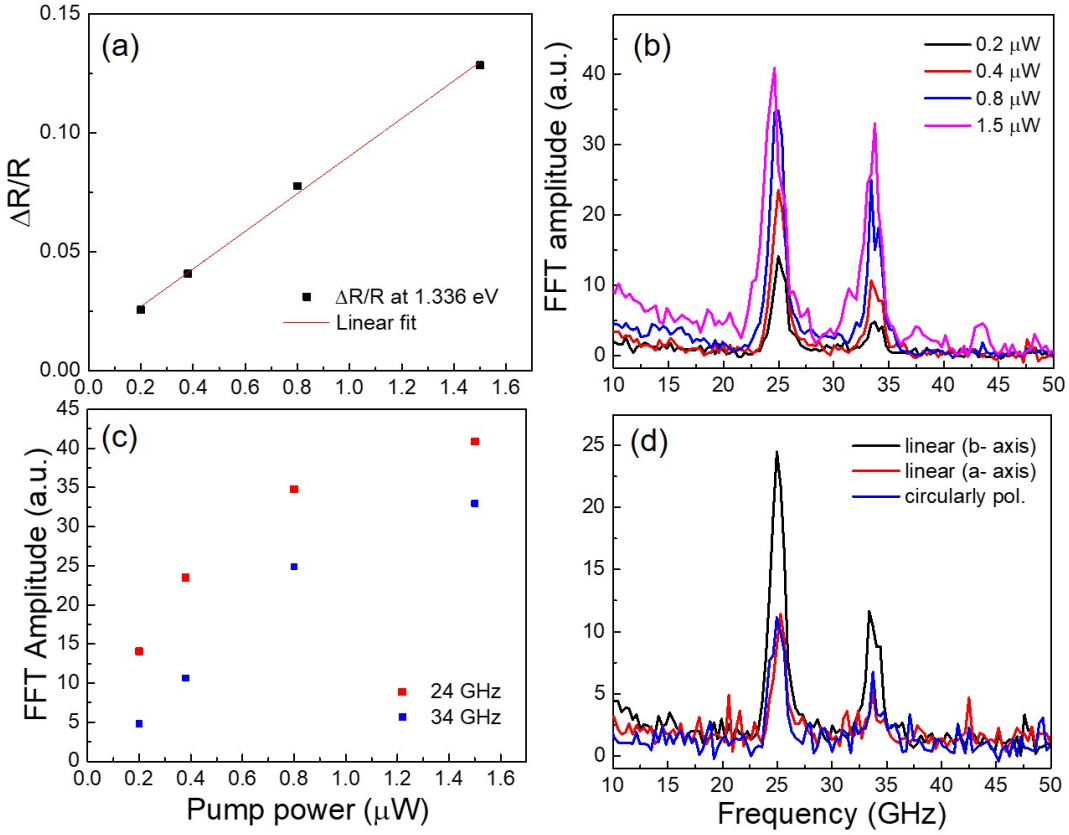

Fig. S21. (a) ΔR/R signal at 1.336 eV vs. pump power. (b) Linearly polarized along the *b*-axis pump power dependent FFT amplitude and (c) the maximum peak amplitude vs. pump power at 24 and 34 GHz. (d) polarization dependent FFT amplitude. Note the same pump power of 0.4 μW is used for different polarizations.

13. Interlayer coupling and single-ion anisotropy value fitting using linear spin wave theory (LSWT).

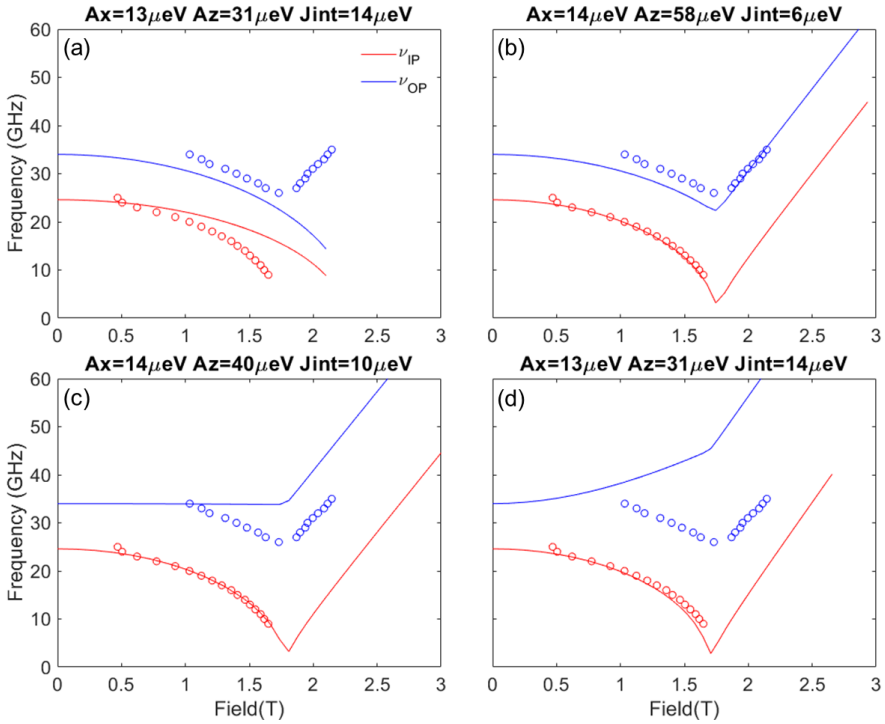

Fig. S22. LSWT fitting of magnetic field dependent AFMR data shown in Fig. 2b in main text using different single ion anisotropy and interlayer exchange constants.

14. Landau-Lifshitz (LL) equation derivation.

In order to understand the three branches from AFMR measurement, we modeled the dynamical spin precession using the LL equation:

$$\frac{d\overrightarrow{m_{(i)}}}{dt} = -\mu_0 \gamma \overrightarrow{m_{(i)}} \times \overrightarrow{H_{eff_{(i)}}} \quad (eq.1)$$

Here, $\vec{m}_{(i)}$ is the magnetic moment where i =1 (top) or 2 (bottom) layer.

We first write down the total energy and use the following equation to find the $\overrightarrow{H_{eff}}$:

$$\overrightarrow{H_{eff_{(i)}}} = \frac{-1}{\mu_0 M_s} \nabla_{\overrightarrow{m_{(i)}}} E_{total} \quad (eq.2)$$

Since CrSBr is a triaxial, AFM system with an easy axis along the b-axis, intermediate axis along the a-axis and hard-axis along c-axis, we consider four energy contributions, Zeeman energy, two different magnetocrystalline anisotropy energy and interlayer exchange energy.

$$E_{total} = -\overrightarrow{m_1} \cdot \overrightarrow{H_{ext,c}} - \overrightarrow{m_2} \cdot \overrightarrow{H_{ext,c}} - \frac{1}{2} H_A m_{b,1}^2 - \frac{1}{2} H_A m_{b,2}^2 - \frac{1}{2} H_B m_{a,1}^2 - \frac{1}{2} H_B m_{a,2}^2$$

$$+ H_E \overrightarrow{m_1} \cdot \overrightarrow{m_2} \quad (eq.3)$$

Here, H_{ext} is applied along the c-axis, $\overrightarrow{m_1}$ and $\overrightarrow{m_2}$ are magnetic moments in the layer 1 and layer 2, respectively, H_A describes the magnetic anisotropy along the easy axis, H_B along the intermediate axis and H_E is the AFM interlayer exchange field. H_A is greater than H_B because b-axis is the easy axis. We ignored a universal factor of $\mu_0 M_s$.

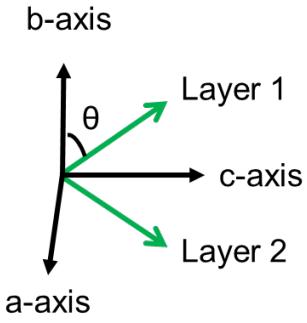

Fig. S23. Magnetic moments represented on a crystallographic axis. θ is an angle between *b* and *c*- axis and φ is an angle between *a* and *c*- axis. The field direction is along the *c*-axis.

Following the coordinate system shown in Figure S17, the total energy can be written down as:

$$E_{total} = -2H_{ext}\sin\theta - H_A cos^2\theta - H_E cos2\theta - H_B(\sin(\theta)\sin(\varphi))^2 \ (eq.4)$$

Taking the derivative with respect to θ and φ,

$$\frac{dE_{total}}{d\theta} = -2H_{ext}\cos(\theta) + 2H_A\cos(\theta)\sin(\theta)\,4H_E\cos(\theta)\sin(\theta) - 2H_B\sin(\theta)\cos(\theta)\sin^2(\varphi) \ (eq.5)$$

$$\frac{dE}{d\varphi} = 2H_B\sin^2(\theta)\sin(\varphi)\cos(\varphi) \quad (eq.6)$$

At equilibrium, $\frac{dE_{total}}{d\theta} = 0$ and $\frac{dE_{total}}{d\varphi} = 0$ gives

$$sin\theta = \frac{H_{ext}}{2H_E + H_A - H_B\sin^2\varphi} \ (eq.7)$$

$$\frac{dE}{d\varphi} = 2H_B\sin^2(\theta)\sin(\varphi)\cos(\varphi) = 0 \quad (eq.8)$$

Since the easy axis is along the *b*-axis, φ = 90° at equilibrium.

Using the eq. 2, $\overrightarrow{H_{eff}}$ for each layer can be written as the following where i and j refer to top and bottom layer:

$$\overrightarrow{H_{eff(\iota=1,2)}} = \overrightarrow{H_{ext,c}} - H_E\overrightarrow{m_j} + H_A m_{b,i}\hat{b} + H_B m_{a,i}\hat{a} \quad (eq.9)$$

We will first find the eigenfrequencies when the out-of-plane field is large enough to saturate both magnetization, $H_{ext,c} > H_s$. In this case, the magnetic moment in AFM coupled layers can be written as, $m_1 \approx \begin{pmatrix} m_{a,1} & 1 & m_{b,1} \end{pmatrix}$ and $m_2 \approx \begin{pmatrix} m_{a,2} & 1 & m_{b,2} \end{pmatrix}$.

Then the effective field and the time derivative of magnetic moment can be written as,

$$\overrightarrow{H_{eff(1)}} = H_{ext,c}\begin{pmatrix}0\\1\\0\end{pmatrix} - H_E\begin{pmatrix}m_{a,2}\\1\\m_{b,2}\end{pmatrix} + H_A\begin{pmatrix}0\\0\\m_{b,1}\end{pmatrix} + H_B\begin{pmatrix}m_{a,1}\\0\\0\end{pmatrix} \ (eq.9)$$

$$\frac{d\overrightarrow{m_1}}{dt} = \begin{pmatrix}m_{a,1}\\0\\m_{b,1}\end{pmatrix} \ (eq.10)$$

where the magnetization has the form of $e^{-i\omega t}$. Plugging these into the eq.1 without a damping term and ignoring the 2nd order and higher terms we get the 4 x 4 matrix:

$$\frac{i\omega}{\mu_0\gamma}\begin{pmatrix} m_{a,1} \\ m_{b,1} \\ m_{a,2} \\ m_{b,2} \end{pmatrix} =$$

$$\begin{pmatrix} 0 & H_A - H_{ext} + H_E & 0 & -H_E \\ H_{ext} - H_E - H_B & 0 & H_E & 0 \\ 0 & -H_E & 0 & H_A - H_{ext} + H_E \\ H_E & 0 & H_{ext} - H_E - H_B & 0 \end{pmatrix} \quad (eq.11)$$

Moving the left term to the right and taking the determinant equals to 0, we can get two eigenfrequencies:

$$f_1 = \frac{\mu_0\gamma}{2\pi}\sqrt{(H_A + 2H_E - H_{ext})(H_B + 2H_E - H_{ext})} \quad (eq.12)$$

$$f_2 = \frac{\mu_0\gamma}{2\pi}\sqrt{(H_A - H_{ext})(H_B - H_{ext})} \quad (eq.13)$$

where f_1 and f_2 corresponds to the in-phase and out-of-phase precession above H_s.

When the external field is below the saturation field, the magnetic moment m_1 and m_2 have the opposite sign. Assuming that $m_1>0$ and $m_2<0$, and the sub-lattice 1 is on the top and sub lattice 2 is at the bottom, we can write magnetic moment in the each other's frame by applying rotation matrix of sublattice 2 respective to sublattice 1:

$$\Gamma_{2,1} = \begin{pmatrix} 1 & 0 & 0 \\ 0 & -\cos(2\theta) & +\sin(2\theta) \\ 0 & -\sin(2\theta) & -\cos(2\theta) \end{pmatrix} \quad (eq.14)$$

Similarly, the rotation matrix from sublattice 1 to sublattice 2 is:

$$\Gamma_{2,1} = \begin{pmatrix} 1 & 0 & 0 \\ 0 & -\cos(2\theta) & +\sin(2\theta) \\ 0 & +\sin(2\theta) & -\cos(2\theta) \end{pmatrix} \quad (eq.15)$$

Applying the rotation matrix to the magnetic moment and solving the eq.1 without a damping term, we obtain the 4 x 4 matrix:

$$\frac{i\omega}{\mu_0\gamma}\begin{pmatrix} m_{a,1} \\ m_{b,1} \\ m_{a,2} \\ m_{b,2} \end{pmatrix} =$$

$$\begin{pmatrix} 0 & -H_E - H_A cos^2(\theta) & 0 & H_E \cos(2\theta) \\ H_E + H_A - H_B & 0 & H_E & 0 \\ 0 & H_E \cos(2\theta) & 0 & -H_E - H_A cos^2(\theta) \\ H_E & 0 & H_E + H_A - H_B & 0 \end{pmatrix} \quad (eq.16)$$

Once again, moving the left term to the right and taking the determinant equals to 0 and using the eq 7, we get the two eigenfrequencies:

$$f_1 = \frac{\mu_0\gamma}{2\pi}\sqrt{(H_A - H_B)(H_A + 2H_E)(1 - \left(\frac{H_{ext}}{(H_A + 2H_E - H_B)}\right)^2)} \quad (eq.17)$$

$$f_2 = \frac{\mu_0\gamma}{2\pi}\sqrt{\begin{matrix}(H_A - H_B + 2H_E)(\left(2H_E - H_A(\left(\frac{H_{ext}}{(H_A + 2H_E - H_B)}\right)^2 - 1)\right) \\ \ldots + 2H_E(\left(\frac{H_{ext}}{(H_A + 2H_E - H_B)}\right)^2 - 1))\end{matrix}} \quad (eq.18)$$

where f_1 and f_2 corresponds to the in-phase and out-of-phase precession below H_s.

At 0 magnetic field, the two eigenfrequencies obtained from LL, (eq. 17) and (eq. 18), become $f_1 = \frac{\mu_0\gamma}{2\pi}\sqrt{(H_A - H_B)(H_A + 2H_E)}$ and $f_2 = \frac{\mu_0\gamma}{2\pi}\sqrt{H_A(H_A - H_B + 2H_E)}$ for ν_{IP} and ν_{OP}, respectively. These equations are complementary to the two eigenfrequencies obtained from LSWT, $2S\sqrt{A_xA_z + A_xJ_{int}}$ and $2S\sqrt{A_xA_z + A_zJ_{int}}$, since H_A H_B, and J_{int} are proportional to (A_z-A_y), (A_z-A_x) and $2H_E$, respectively. Since A_y is set to 0 during LSWT fitting, we can recover the

same equations by replacing anisotropy and exchange field to single ion anisotropy and exchange constants.

Although we expect to see 4 branches as described in the 4 eigenfrequencies, we only observe three branches without the in-phase precession branch after saturation field. This is persistent throughout all temperature ranges. We suspect that due to some symmetry constraint, we cannot detect this branch, similar to that observed in $CrCl_3$.[6] We fit three branches using the three eigenfrequencies described in eq 12, 17 and 18. We obtain consistent exchange (H_E) and anisotropy fields (H_A and H_B) from fitting different branches and they match well with the measured anisotropy fields from magnetic isotherm (Table S4). The electron gyromagnetic ratio term, $\frac{\mu_0\gamma}{2\pi}$ slightly deviates from the expected value, 28 GHz/T at different temperatures (Tables S2-S4). Presumably, ignoring higher order terms could lead to slightly lower value of gyromagnetic ratio. This is also observed in LSWT fitting as discussed above.

Table S2. LLG fit parameters for the out-of-phase precession below the saturation field

Temperature (K)	$\gamma/2\pi$ (T)	H_E (T)	H_A (T)	H_B (T)
5	24.9	0.26	1.60	0.64
20	28	0.22	1.3	0.5
40	27	0.14	1.5	0.8
60	26	0.13	1.4	0.8
80	27	0.12	1.0	0.3
100	28	0.11	0.69	0.2

Table S3. LLG fit parameters for the in-phase precession below the saturation field

Temperature (K)	$\gamma/2\pi$ (T)	H_E (T)	H_A (T)	H_B (T)
5 (AFMR)	16.8	0.27	1.6	0.50
5 (Optical)	28	0.16	1.4	1.0
20	28	0.24	1.2	0.77
40	25	0.20	1.1	0.64
60	21	0.10	1.2	0.6
80	27	0.2	0.78	0.48
100	21	0.10	0.72	0.33

Table S4. LLG fit parameters for the out-of-phase precession above the saturation field

Temperature (K)	$\gamma/2\pi$ (T)	H_A (T)	H_B (T)
5	23	1.3	0.5
20	21	1.2	0.8
40	22	1.0	0.46
60	22	1.2	0.65
80	21	0.83	0.34
100	24	0.53	0.44

15. Vibrating sample magnetometry. Vibrating sample magnetometry (VSM) measurements were conducted on a Quantum Design PPMS DynaCool system. Two single crystals of CrSBr were co-aligned and attached to a quartz paddle using GE varnish with the crystallographic a-axis aligned parallel to the length of the quartz paddle, which coincides with the direction of the applied field. Variable-field magnetization curves were collected from 0 to 5 T (20 Oe/s). For each temperature, one linear fit was applied to the high-field data ($H > 2$ T), above the saturation field, and a second linear fit was applied to the linear region at low fields. The intersection of these two lines yields the anisotropy field for the *a*-axis as its abscissa. To obtain the c-axis anisotropy fields, the crystals were then removed from the quartz paddle and re-attached to the paddle with the *c*-axis aligned parallel to the field direction.

Table S5. Anisotropy fields at different temperatures

Temperature (K)	H_A-H_B (*a*-axis) T	H_A (*c*-axis) T
2	1.054	1.661
10	1.027	1.647
20	0.979	1.597
30	0.924	1.532
40	0.887	1.474
50	0.827	1.397
60	0.771	1.330
70	0.723	1.243
80	0.655	1.156
90	0.592	1.071
100	0.524	0.965
110	0.480	0.852
120	0.388	0.731
130	0.284	0.582

Reference

1. Wang, J. *et al.* Optical generation of high carrier densities in 2D semiconductor heterobilayers. *Sci. Adv.* **5**, eaax0145 (2019).
2. Wang, J. *et al.* Diffusivity Reveals Three Distinct Phases of Interlayer Excitons in MoSe2/WSe2 Heterobilayers. *Phys. Rev. Lett.* **126**, 106804 (2021).
3. Holstein, T. & Primakoff, H. Field Dependence of the Intrinsic Domain Magnetization of a Ferromagnet. *Phys. Rev.* **58**, 1098–1113 (1940).
4. Toth, S. & Lake, B. Linear spin wave theory for single-Q incommensurate magnetic structures. *J. Phys. Condens. Matter* **27**, 166002 (2015).
5. Scheie, A. *et al*. Spin waves and magnetic exchange Hamiltonian in CrSBr. *arXiv preprint arXiv:2204.12461* (2022).
6. MacNeill, D. *et al.* Gigahertz Frequency Antiferromagnetic Resonance and Strong Magnon-Magnon Coupling in the Layered Crystal CrCl3. *Phys. Rev. Lett.* **123**, 47204 (2019).